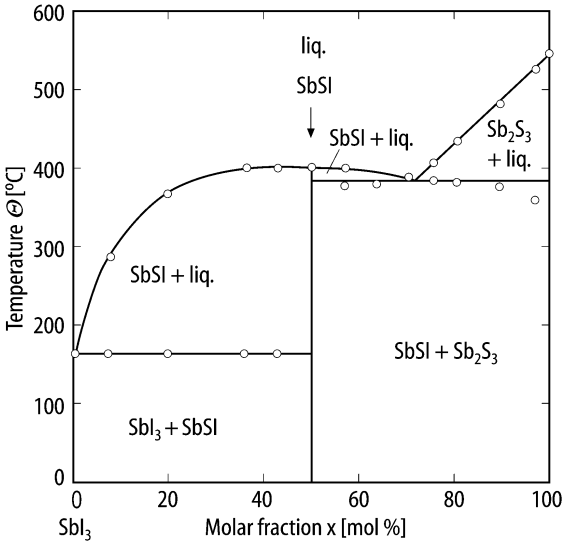

Fig. 20A-7-001. SbSI. Θ vs. x [64Mor]. Phase diagram of SbI_3-Sb_2S_3 system.

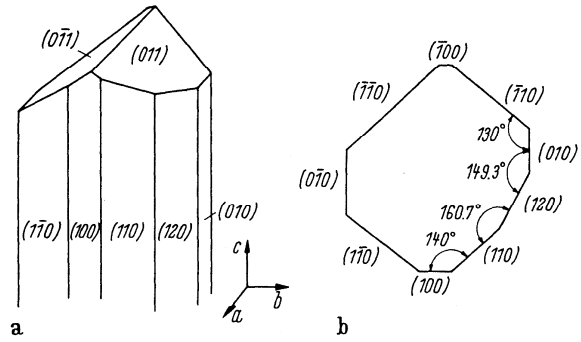

Fig. 20A-7-002. SbSI. (**a**) Crystal form [64Mor]. (**b**) Cross section perpendicular to the *c* axis [67Kik].

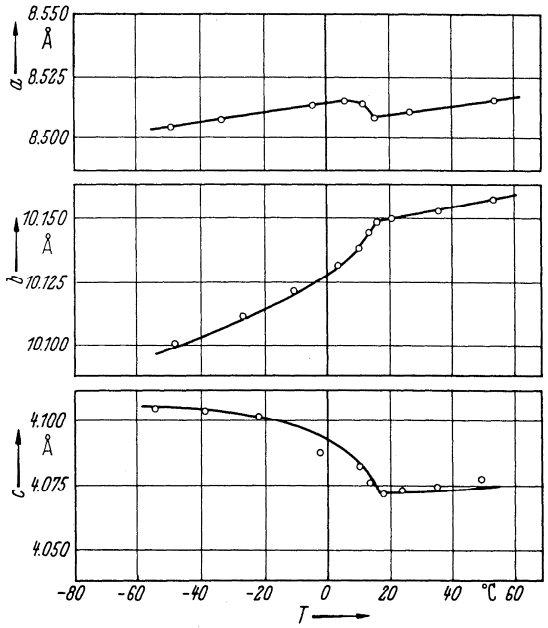

Fig. 20A-7-003. SbSI. *a, b, c* vs. *T* [64Fut]. *a*, *b*, and *c* are determined from (10,0,0), (0,12,0) and (0,0,4) reflections, respectively.

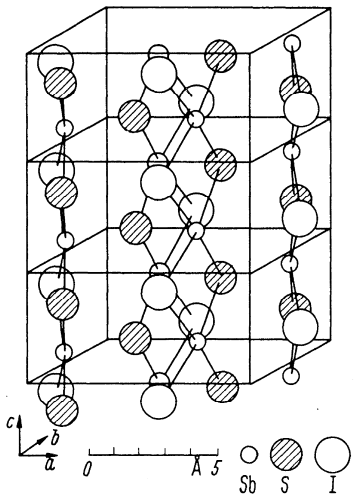

Fig. 20A-7-004. SbSI. Crystal structure of phase I [50Don].

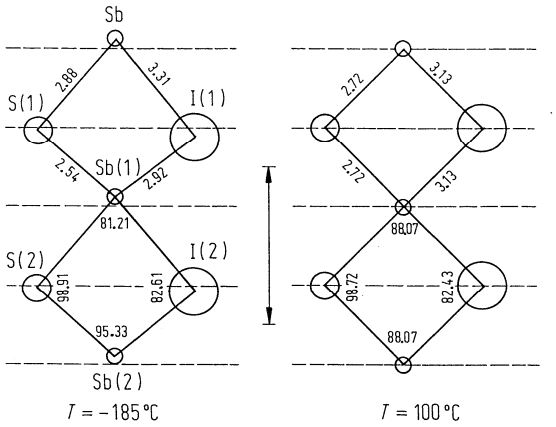

Fig. 20A-7-005. SbSI. Structure [76Iwa]. Interatomic distances [Å] and bond angles [°] at –185 °C and 100 °C. See also Table 20A-7-006.

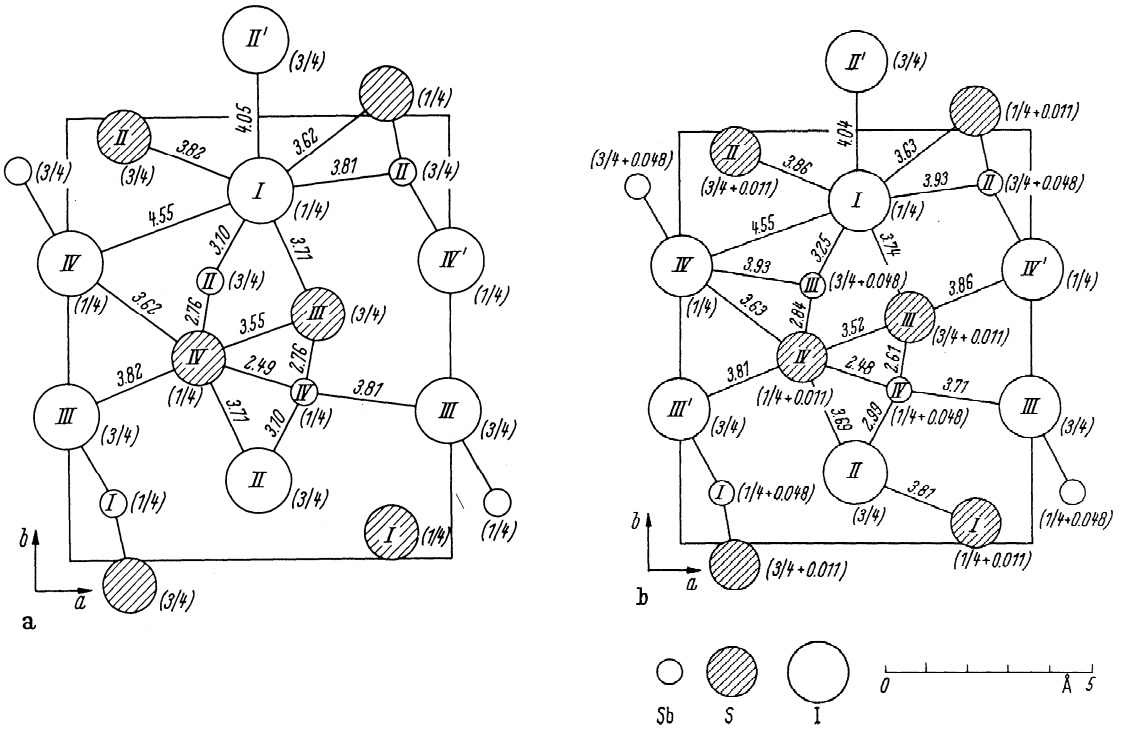

Fig. 20A-7-006. SbSI. Projections of atoms along *c* [67Kik]. Interatomic distances [Å] and *z* parameters of each atom are shown. (**a**) phase I at 35 °C. (**b**) phase II at 5 °C. See also Table 20A-7-005.

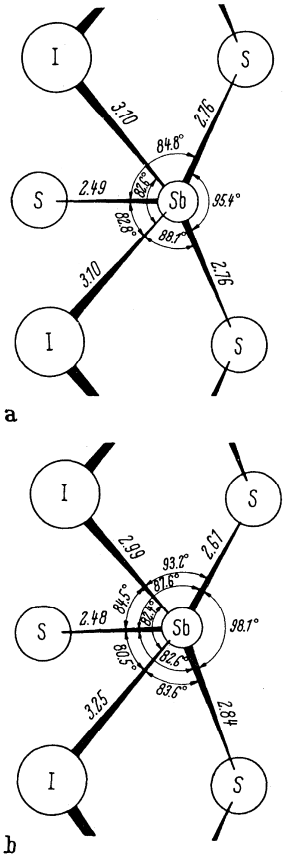

Fig. 20A-7-007. SbSI. Shapes of SbSl molecule [67Kik]. (**a**) phase I at 35 °C. (**b**) phase II at 5 °C.

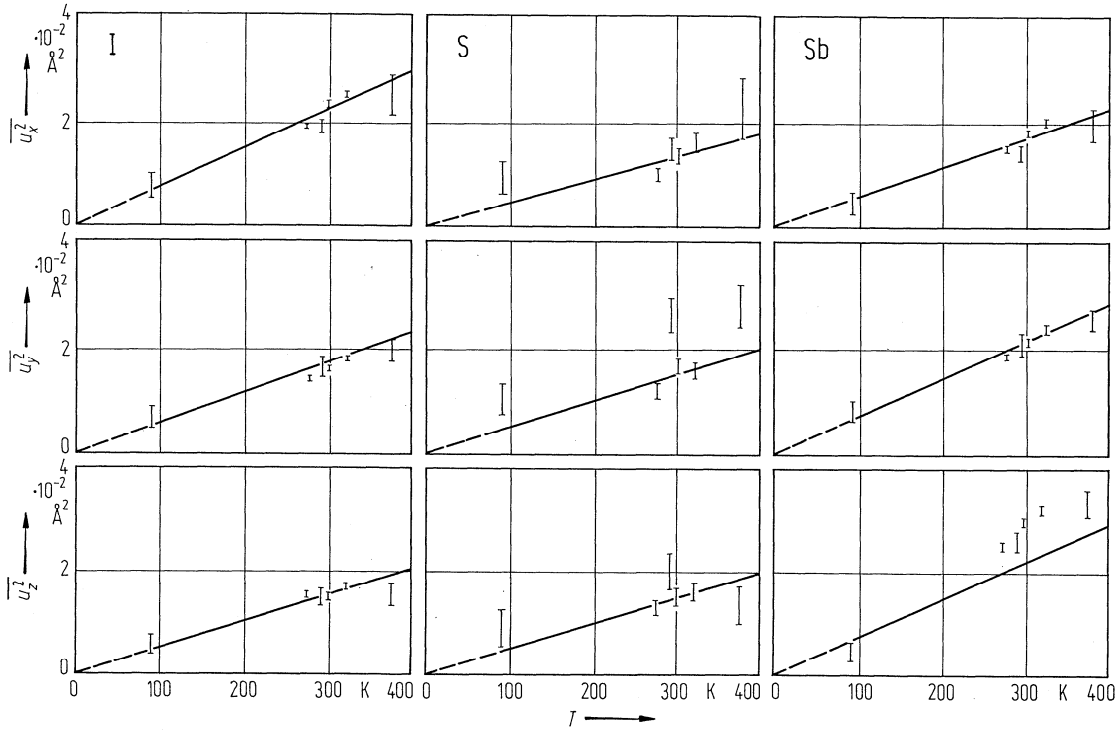

Fig. 20A-7-008. SbSI. Mean-square amplitudes of thermal vibrations vs. *T* [80Ito]. The values are along the orthorhombic axes.

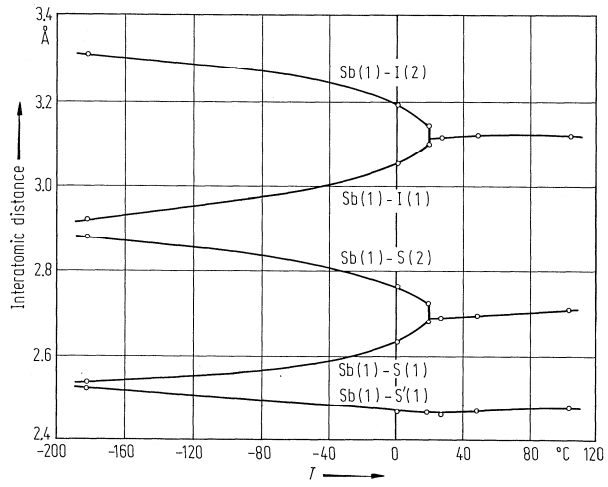

Fig. 20A-7-009. SbSI. Interatomic distances vs. *T* [80Ito]. Data are quoted from [74Ito], [76Ito] and [76Iwa].

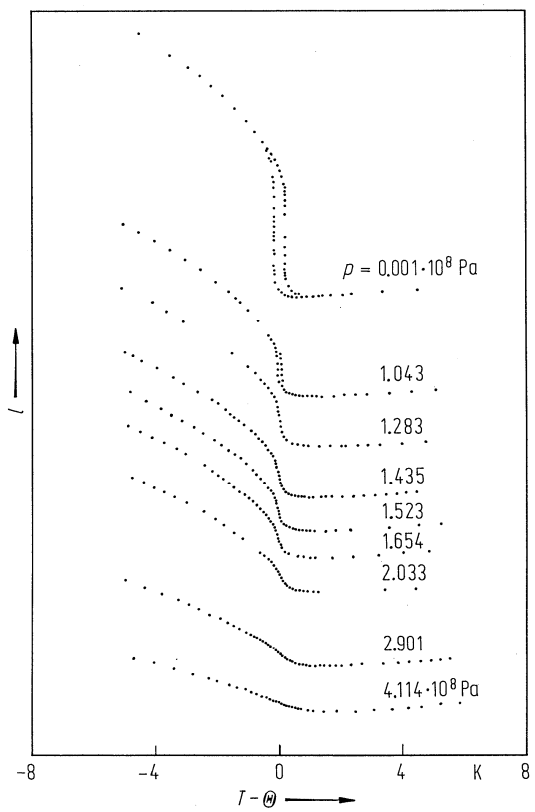

Fig. 20A-7-010. SbSI. l vs. $(T - \Theta)$ [79Zis]. l: length of sample crystal along the c axis. Parameter: p.

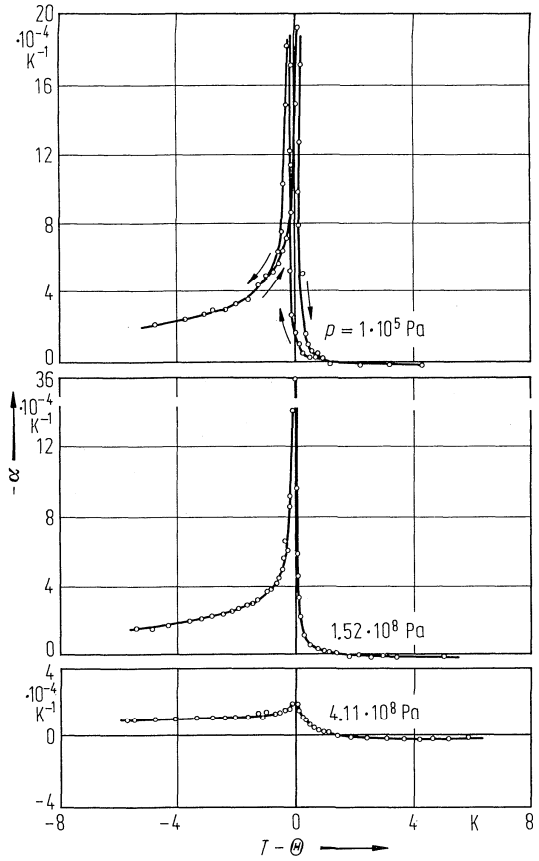

Fig. 20A-7-011. SbSI. α vs. $(T - \Theta)$ [79Zis]. α: linear thermal expansion coefficient along the *c* axis. Parameter: *p*.

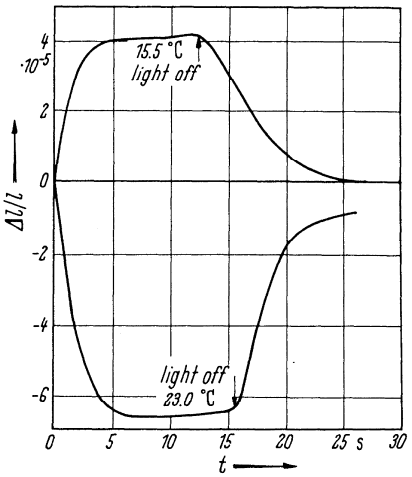

Fig. 20A-7-012. SbSI. $\Delta l/l$ vs. *t*. Strain relaxation curve due to light illumination ($\lambda \cong 450$ nm) under a dc field ($E = 100$ kV m^{-1}) along the *c* axis [66Tat].

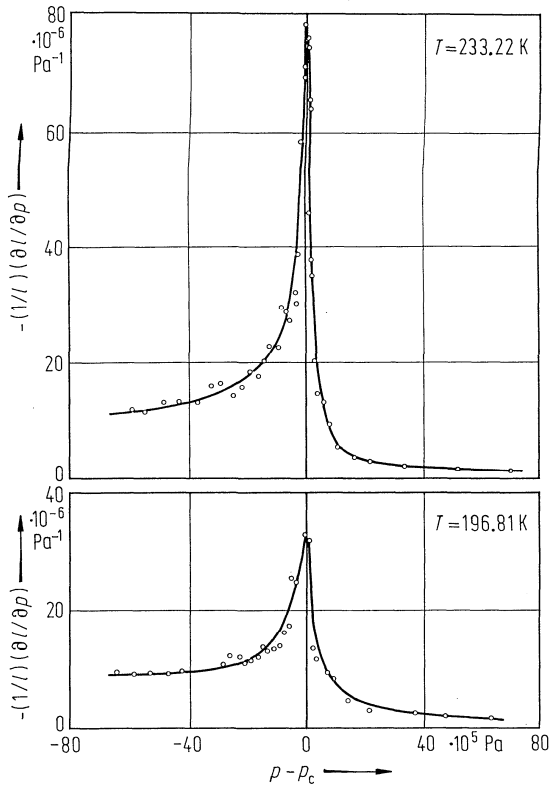

Fig. 20A-7-013. SbSI. $-l^{-1} \cdot \partial l/\partial p$ vs. $(p - p_c)$ [79Zis]. $-l^{-1} \cdot \partial l/\partial p$: linear compressibility along the c axis, p_c: critical pressure to cause the phase transition. Parameter: T.

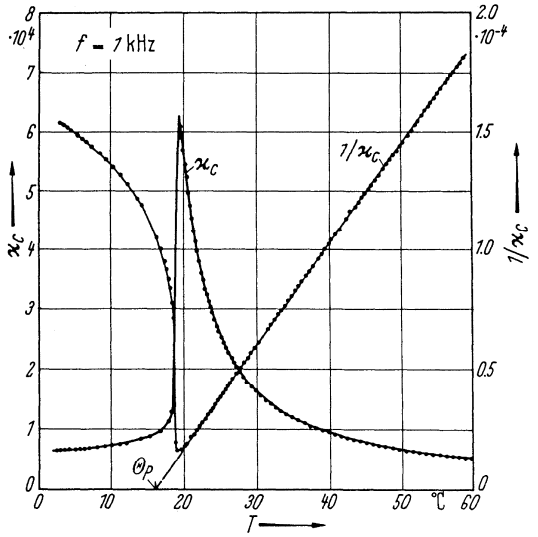

Fig. 20A-7-014. SbSI. κ_c, $1/\kappa_c$ vs. T [64Mor].

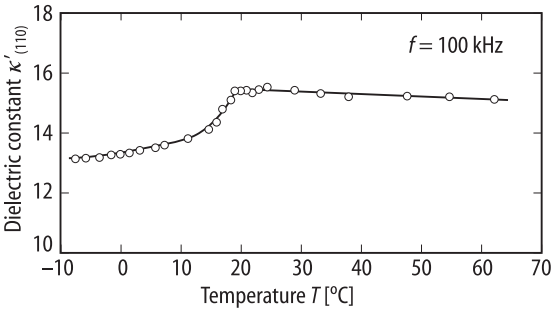

Fig. 20A-7-015. SbSI. $\kappa'_{(110)}$ vs. T [78Iri]. $\kappa'_{(110)}$: dielectric constant measured in the direction perpendicular to (110).

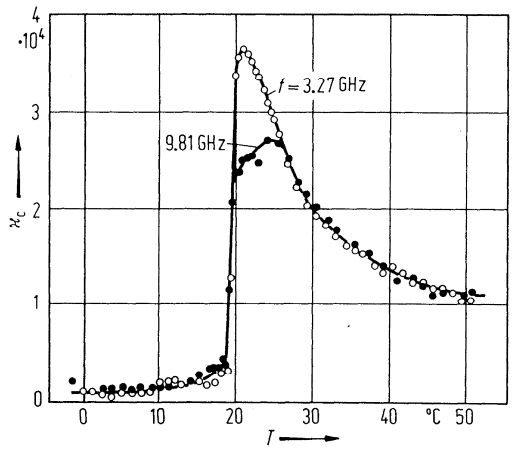

Fig. 20A-7-016. SbSI. κ_c vs. T at microwave frequencies [70Hos]. Parameter: f.

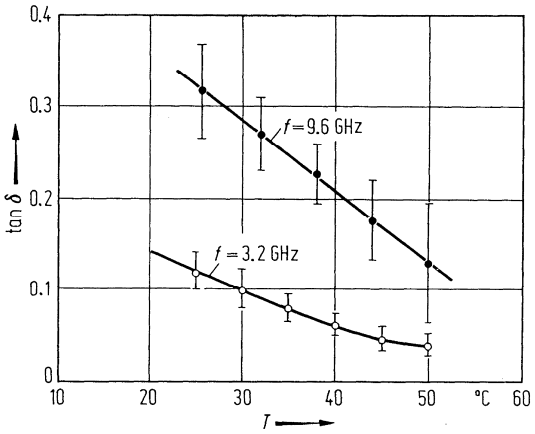

Fig. 20A-7-017. SbSI. tan δ vs. T at microwave frequencies [70Hos]. Parameter: f.

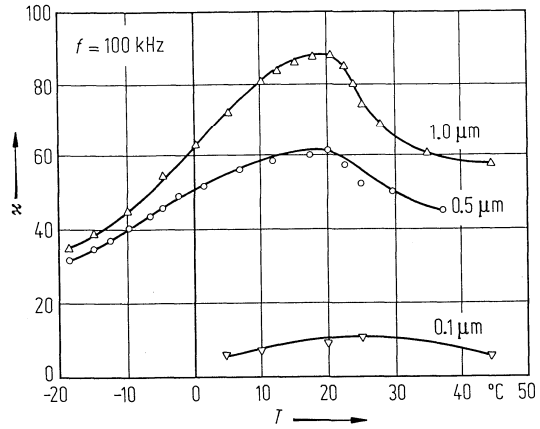

Fig. 20A-7-018. SbSI (thin film). κ vs. T [85Sud]. Parameter: film thickness.

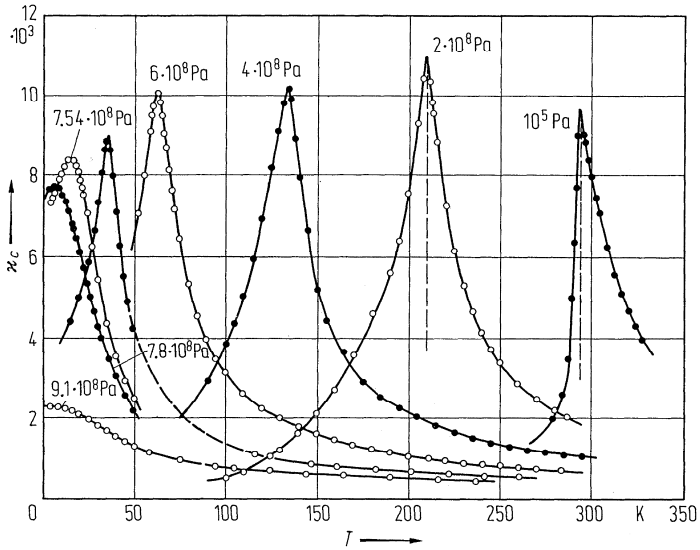

Fig. 20A-7-019. SbSI. κ_c vs. T [75Sam]. Parameter: p, hydrostatic pressure. κ_c at f = 1…100 kHz.

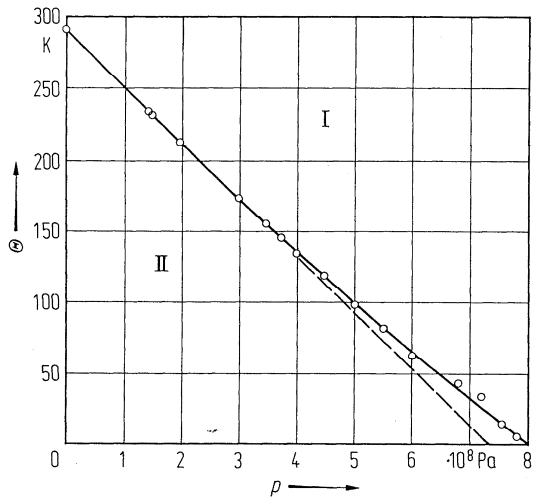

Fig. 20A-7-020. SbSI. Θ vs. p [75Sam].

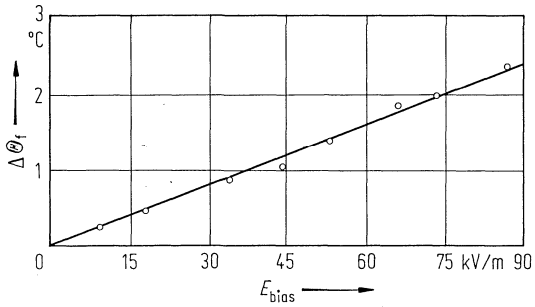

Fig. 20A-7-021. SbSI. $\Delta\Theta_f$ vs. E_{bias} [86Toy]. $\Delta\Theta_f$: shift of Curie temperature.

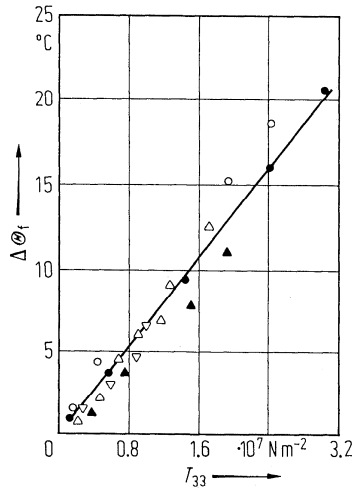

Fig. 20A-7-022. SbSI. $\Delta\Theta_f$ vs. T_{33} [72Vol]. $\Delta\Theta_f$: shift of the ferroelectric Curie temperature. Different symbols correspond to different specimens.

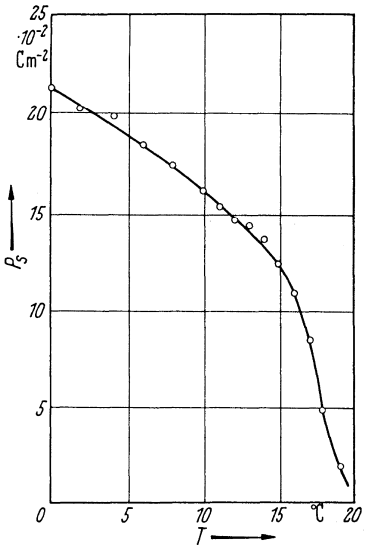

Fig. 20A-7-023. SbSI. P_s vs. T [62Fat]. P_s is estimated from D–E hysteresis loops at 50 Hz.

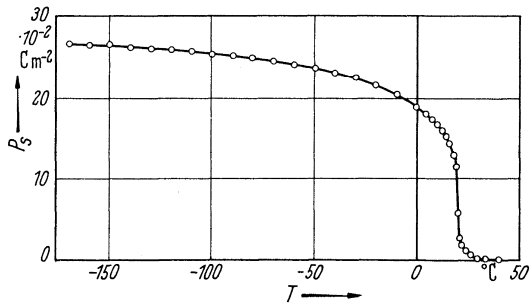

Fig. 20A-7-024. SbSI. P_s vs. T [66Ima]. P_s is estimated from the pyroelectric discharge.

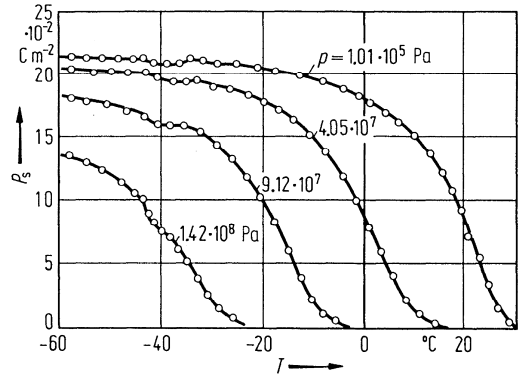

Fig. 20A-7-025. SbSI. P_s vs. T [68Ger]. Parameter: p.

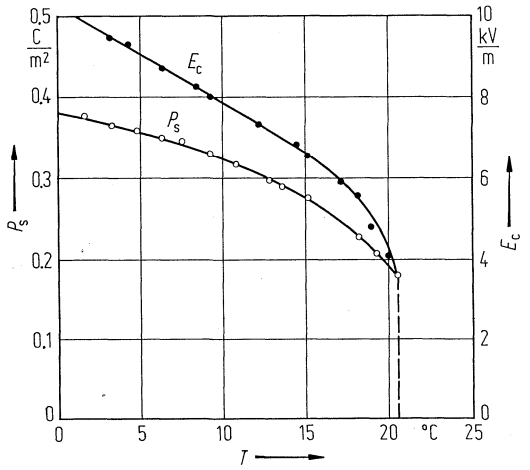

Fig. 20A-7-026. SbSI. P_s, E_c vs. T [86Toy].

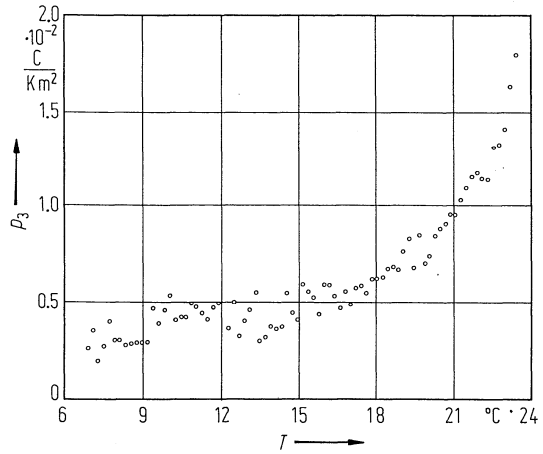

Fig. 20A-7-027. SbSI (single crystal fiber). p_3 vs. T [81Bha]. p_3: pyroelectric coefficient along [001] axis.

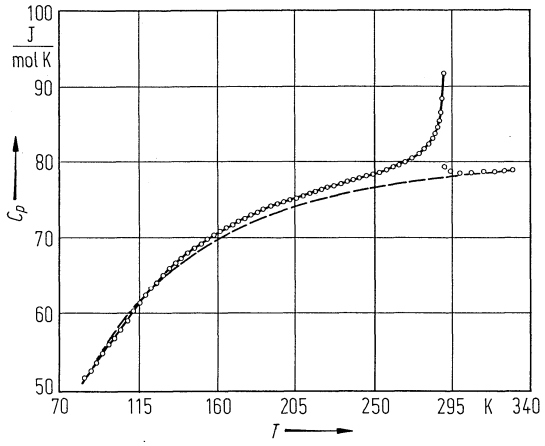

Fig. 20A-7-028. SbSI. C_p vs. T [81Sto]. C_p: molar heat capacity at constant pressure.

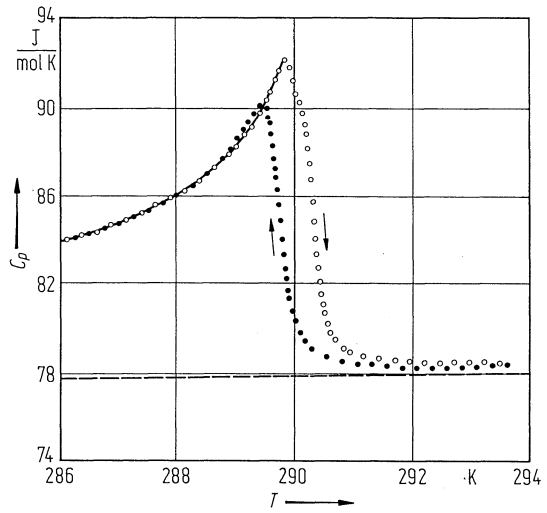

Fig. 20A-7-029. SbSI. C_p vs. T [81Sto]. C_p: molar heat capacity at constant pressure.

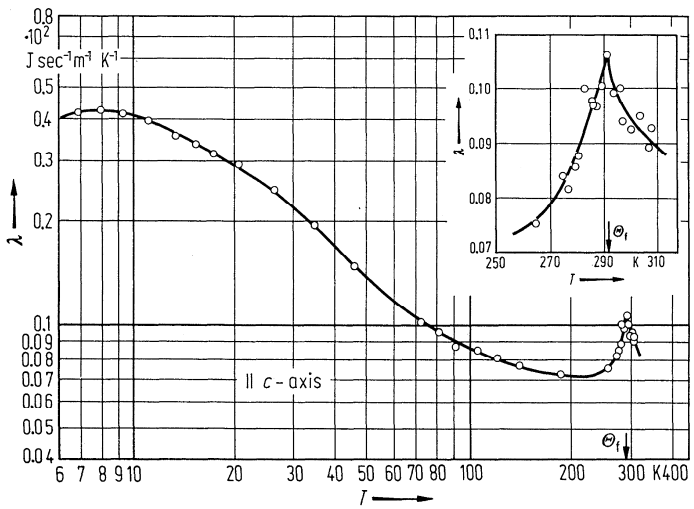

Fig. 20A-7-030. SbSI. λ_c vs. T [68Stu]. λ_c: thermal conductivity along the c axis.

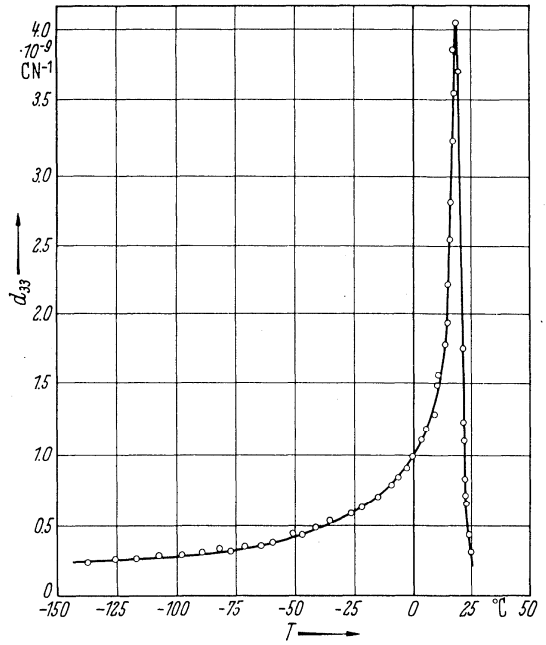

Fig. 20A-7-031. SbSI. d_{33} vs. T [65Ham].

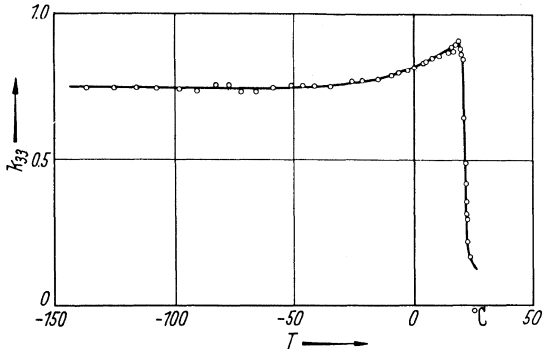

Fig. 20A-7-032. SbSI. k_{33} vs. T [65Ham].

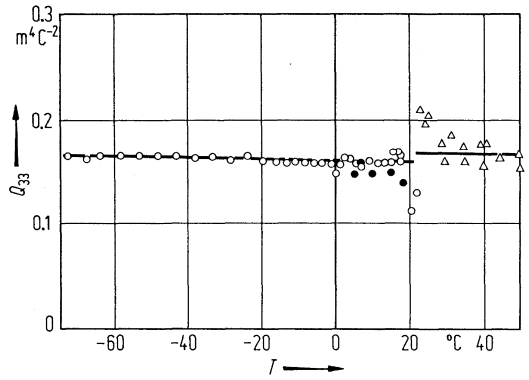

Fig. 20A-7-033. SbSI. Q_{33} vs. T [72Ham]. Q_{33}: electrostrictive constant obtained by three different methods.

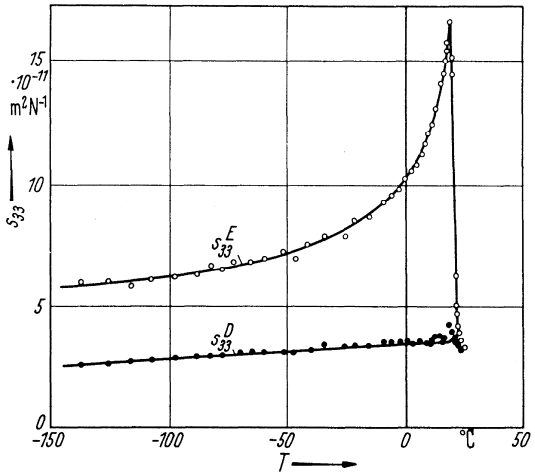

Fig. 20A-7-034. SbSI. s_{33}^{E}, s_{33}^{D} vs. T [65Ham].

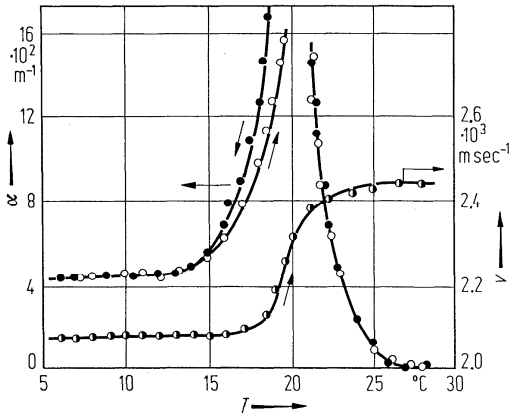

Fig. 20A-7-035. SbSI. α, v vs. T [71Sam]. α, v: absorption coefficient and velocity for 10 MHz quasi-longitudinal ultrasound wave propagating along the c axis, respectively.

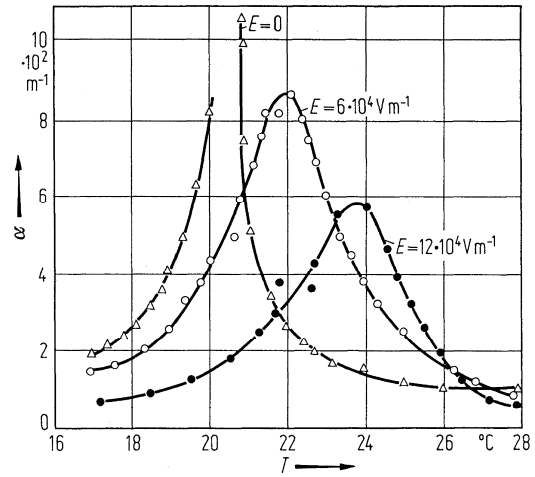

Fig. 20A-7-036. SbSI. α vs. T [69Sam]. Parameter: E, dc bias field parallel to the c axis. α: absorption coefficient of a longitudinal wave at 10 MHz propagating along the c axis.

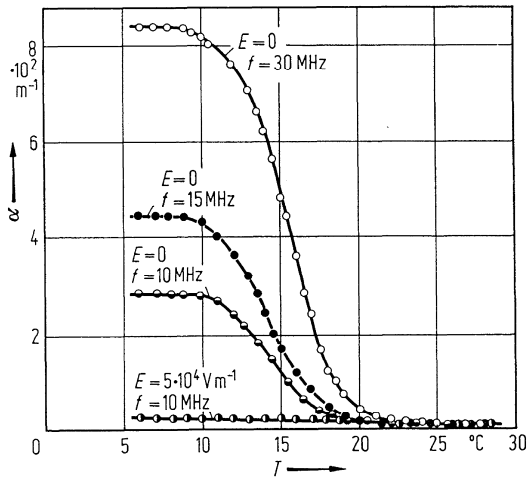

Fig. 20A-7-037. SbSI. α vs. T [71Sam]. Parameters: E, dc bias field parallel to the c axis, and f. α: absorption coefficient of quasi-transverse ultrasonic wave propagating perpendicular to the c axis.

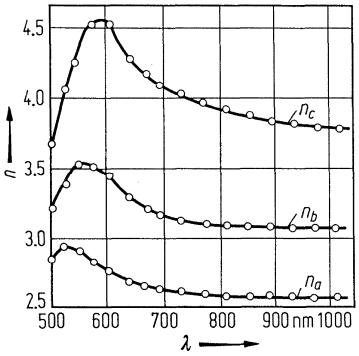

Fig. 20A-7-038. SbSI. n vs. λ [68Ger].

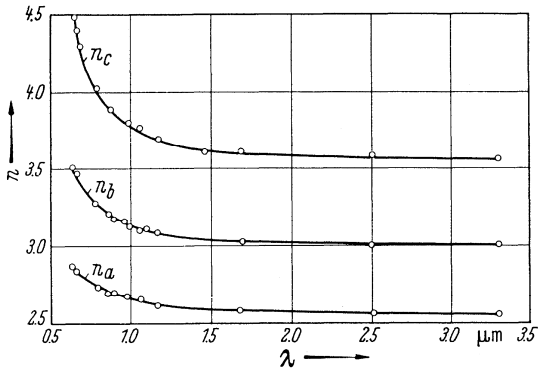

Fig. 20A-7-039. SbSI. n vs. λ [67Joh].

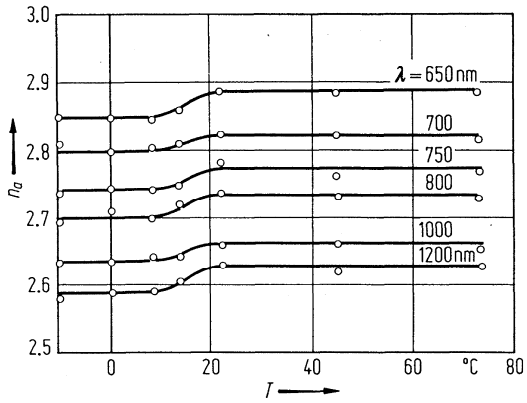

Fig. 20A-7-040. SbSI. n_a vs. T [70Ohi]. Parameter: λ.

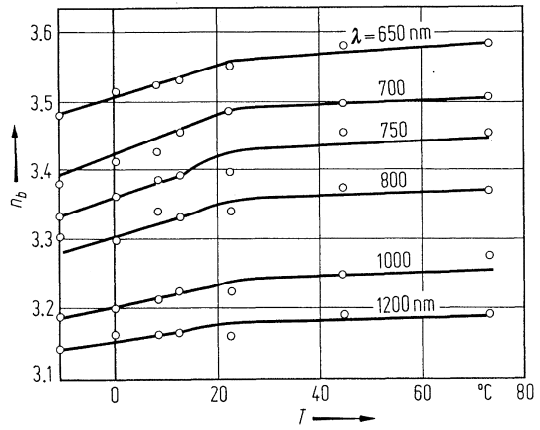

Fig. 20A-7-041. SbSI. n_b vs. T [70Ohi]. Parameter: λ.

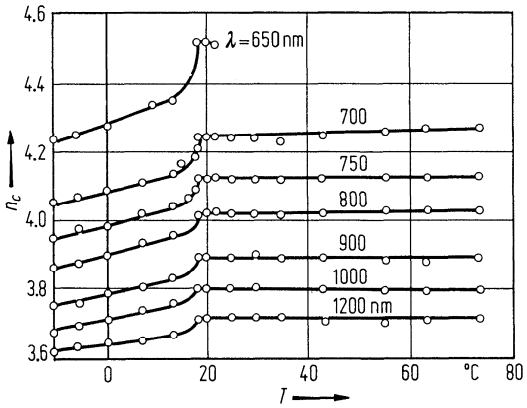

Fig. 20A-7-042. SbSI. n_c vs. T [70Ohi]. Parameter: λ.

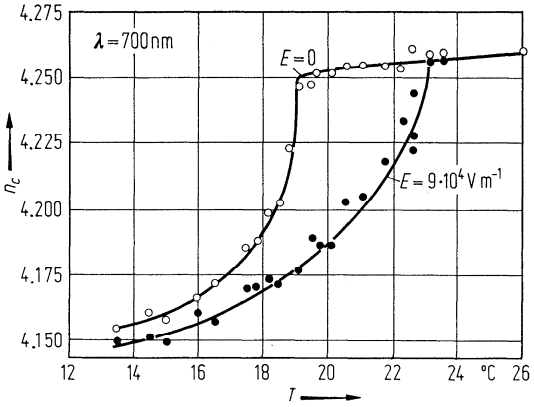

Fig. 20A-7-043. SbSI. n_c vs. T [70Ohi]. Parameter: E, dc bias field.

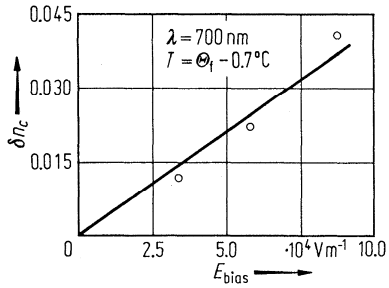

Fig. 20A-7-044. SbSI. δn_c vs. E_{bias} at $\lambda = 700$ nm, at 0.7 °C below Θ_f [70Ohi]. $\delta n_c = n_c(E_{bias} = 0) - n_c(E_{bias})$.

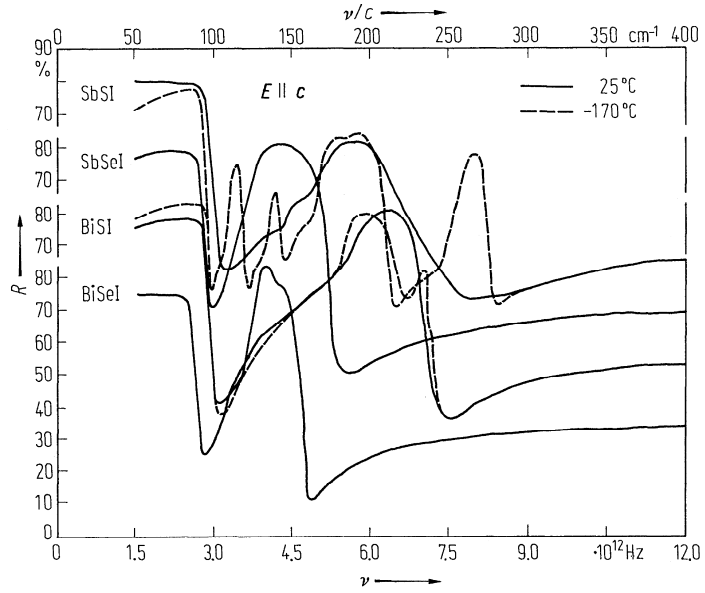

Fig. 20A-7-045. SbSI, BiSI, SbSeI, BiSeI. R vs. ν at 25 °C and –170 °C [73Pet]. R: reflectivity. ν: frequency of the incident infrared radiation polarized parallel to the c axis.

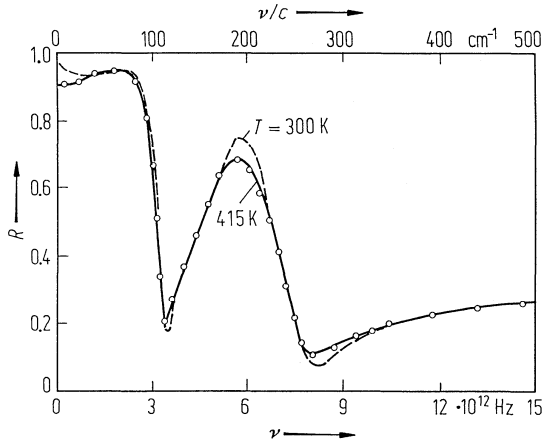

Fig. 20A-7-046. SbSI. *R* vs. *ν* at 415 K and 300 K [82Mas]. *R*: reflectivity. Electric field is parallel to the *c* axis. Full line: calculation.

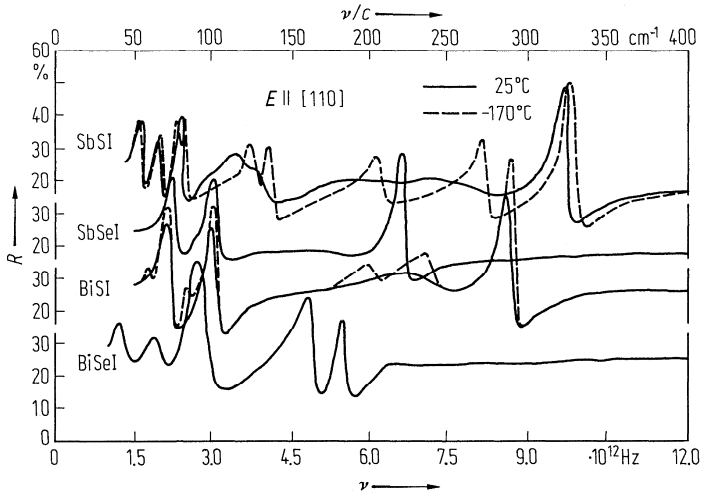

Fig. 20A-7-047. SbSI, BiSI, SbSeI, BiSeI. *R* vs. *ν* at 25 °C and –170 °C [73Pet]. Incident light polarized parallel to [110].

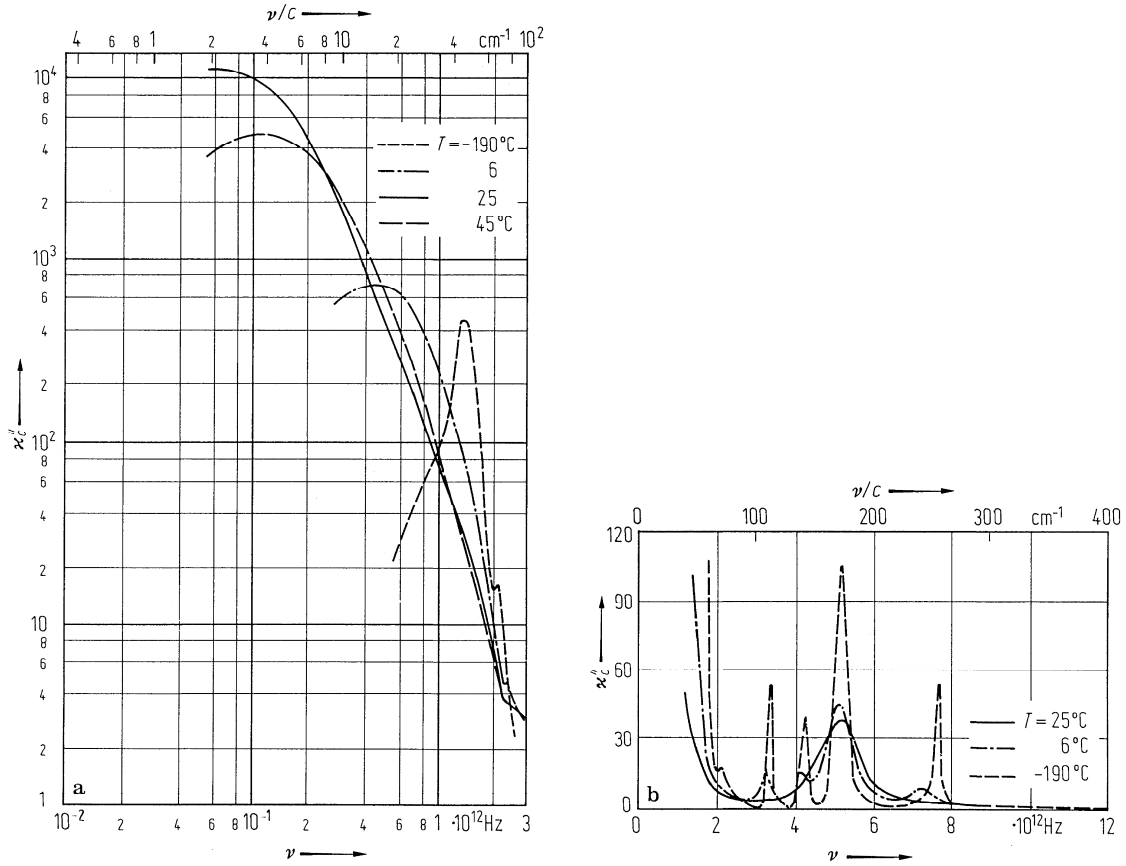

Fig. 20A-7-048. SbSI. κ_c'' vs. ν [72Sug]. Parameter: T. κ_c'' data were obtained from reflectivity by using Kramers-Kronig relation.

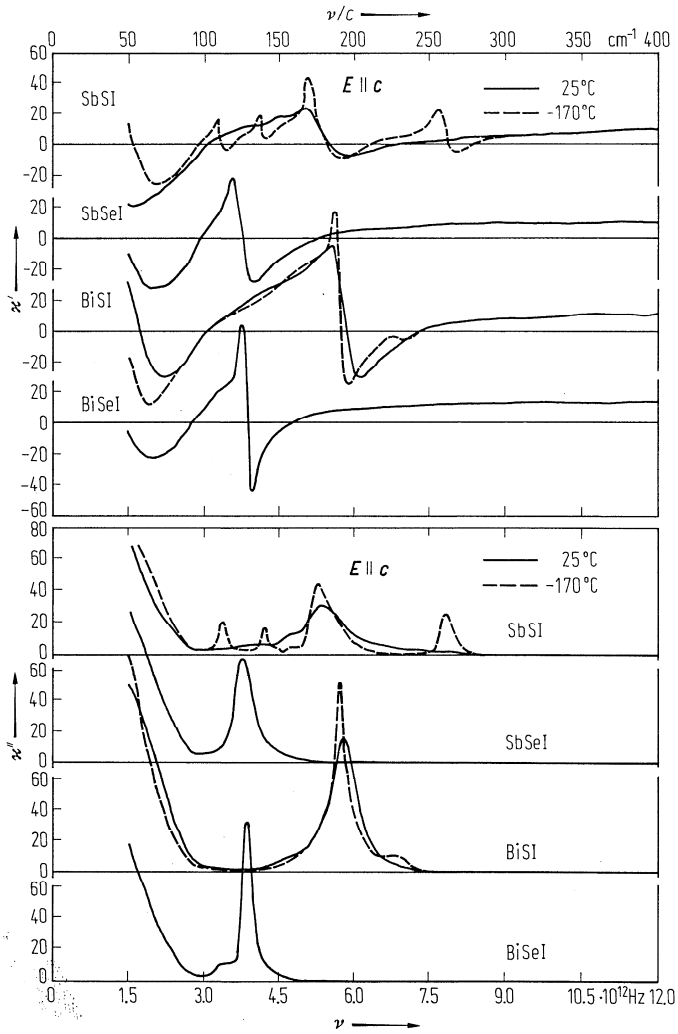

Fig. 20A-7-049. SbSI, BiSI, SbSeI, BiSeI. κ' , κ'' vs. ν for infrared radiation polarized parallel to the c axis [73Pet].

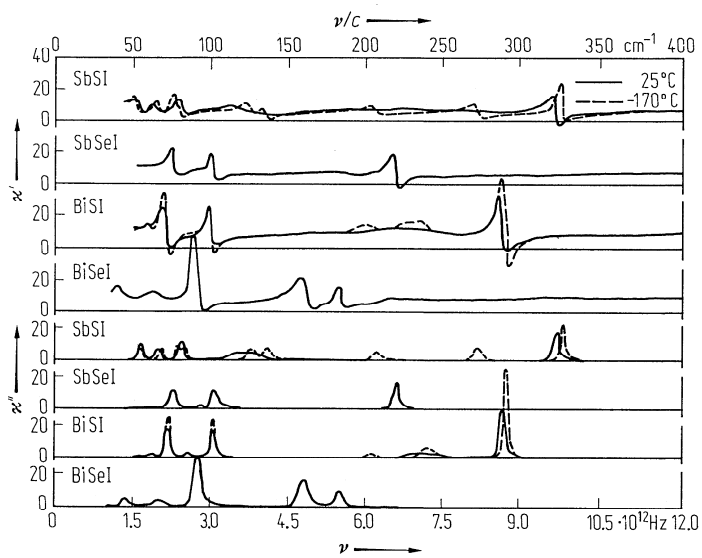

Fig. 20A-7-050. SbSI, BiSI, SbSeI, BiSeI. κ' , κ'' vs. ν for radiation polarized parallel to (110) plane [73Pet].

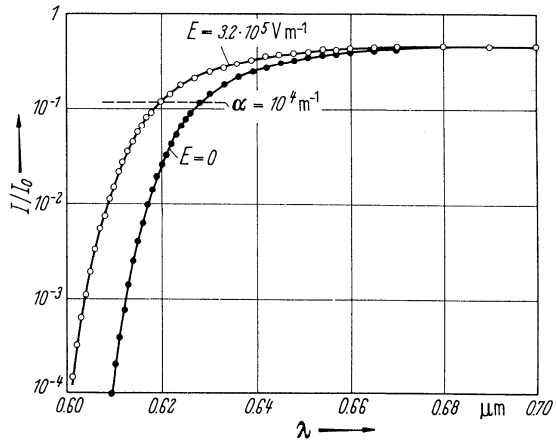

Fig. 20A-7-051. SbSI. Optical transmission I/I_0 vs. λ for unpolarized light at 22 °C [62Ker]. Parameter: dc bias field along the c axis.

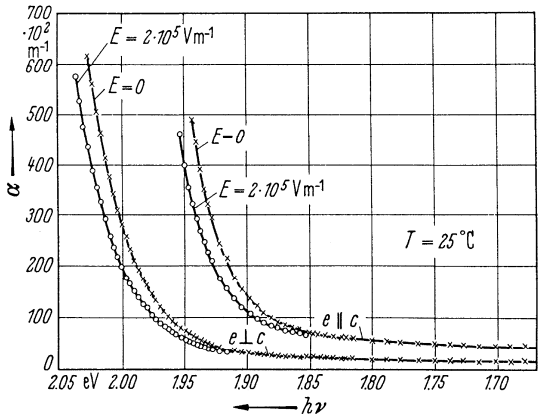

Fig. 20A-7-052. SbSI. Absorption coefficient α vs. $h\nu$ at 25 °C [63Har]. Parameter: applied dc field along the c axis. e: electric field vector of the incident polarized light.

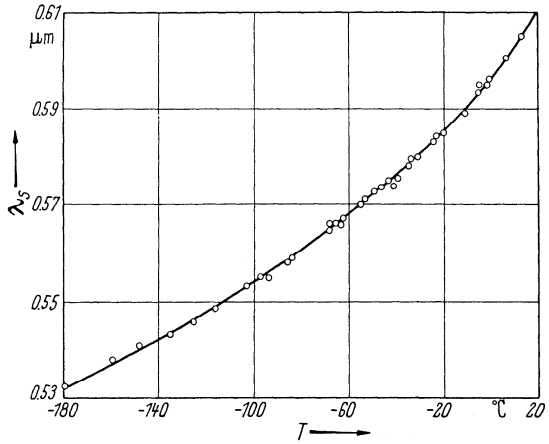

Fig. 20A-7-053. SbSI. Absorption edge λ_s vs. T [62Ker]. λ_s: the threshold wave length where the crystal becomes non-transparent.

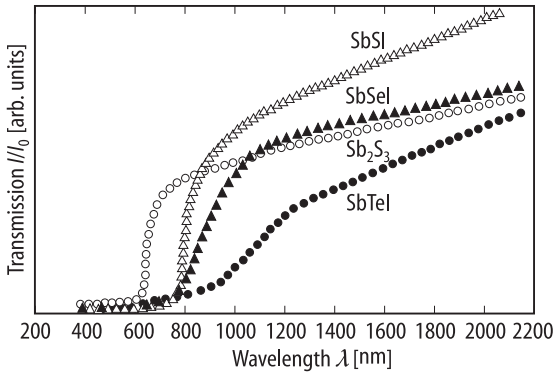

Fig. 20A-7-054. SbSI, SbSeI, SbTeI, Sb_2S_3. I/I_0 vs. λ [84Iba]. I/I_0: transmission.

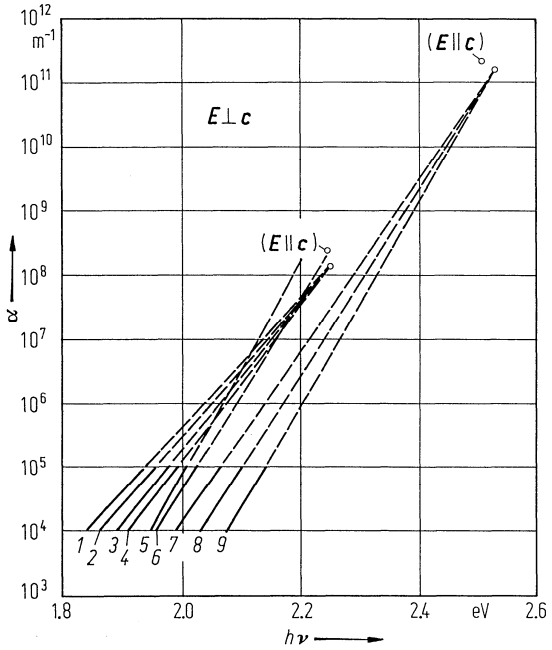

Fig. 20A-7-055. SbSI. α vs. $h\nu$ [84Zam]. α: optical absorption coefficient. Parameter: *T*; *1*: 371 K; *2*: 354 K; *3*: 323 K; *4*: 308 K; *5*: 290 K; *6*: 287 K; *7*: 274.5 K; *8*: 254.5 K; *9*: 230 K. *E*: electric field.

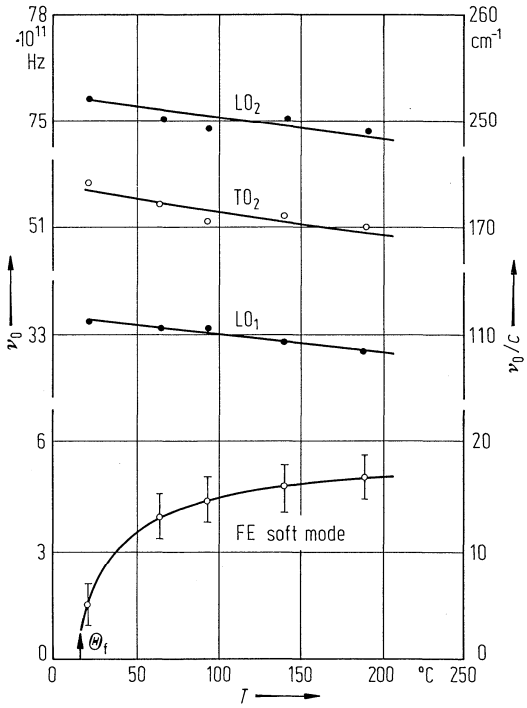

Fig. 20A-7-056. SbSI. v_0 vs. T [82Mas]. v_0: frequency of lattice vibration modes obtained from infrared spectra.

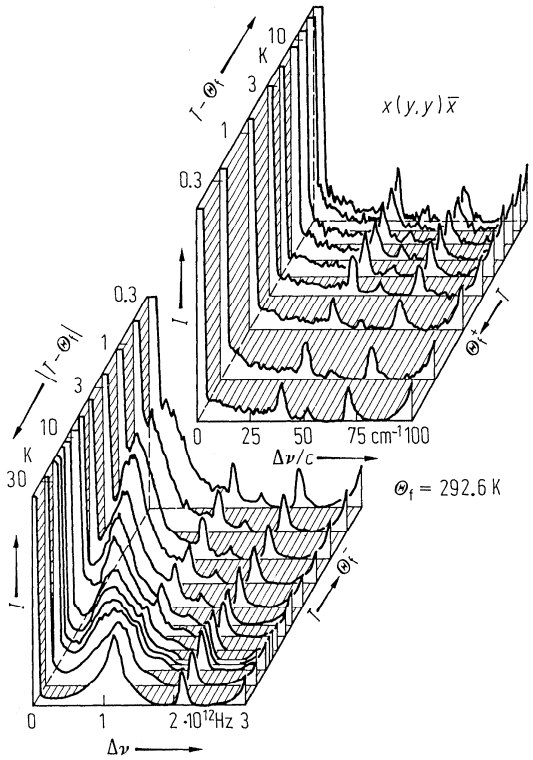

Fig. 20A-7-057. SbSI. I vs. $\Delta\nu$ [75Ste]. Parameter: T. I: Raman scattering intensity for the polarization geometry of $x(yy)\bar{x}$. $\Delta\nu$: frequency shift. The front part of the figure is for the ferroelectric phase and the back is for the paraelectric phase.

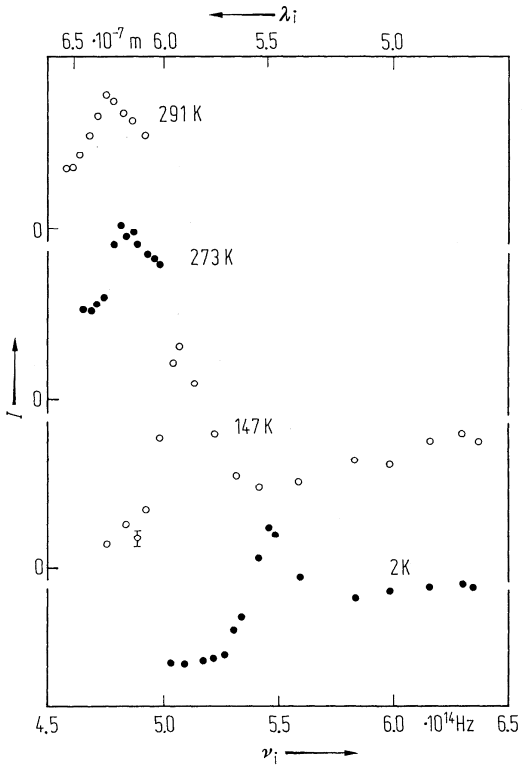

Fig. 20A-7-058. SbSI. I vs. ν_i [76Ame]. Parameter: T. I: Raman scattering intensity of the 112 cm^{-1} mode. ν_i: frequency of incident light. The peaks indicate that the scattering is enhanced when ν_i is near the absorption edge. Refer also to [71Agr].

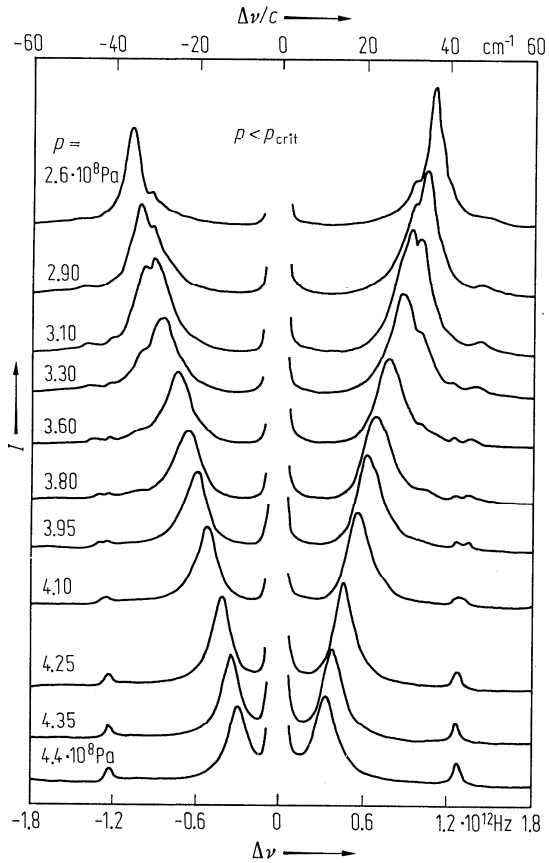

Fig. 20A-7-059. SbSI. I vs. $\Delta\nu$ [76Pee]. Parameter: hydrostatic pressure p. I: Raman scattering intensity at 119 K. $\Delta\nu$: frequency shift. The transition pressure at this temperature is $p_{crit} = 4.54 \cdot 10^8$ Pa. See also [75Pee].

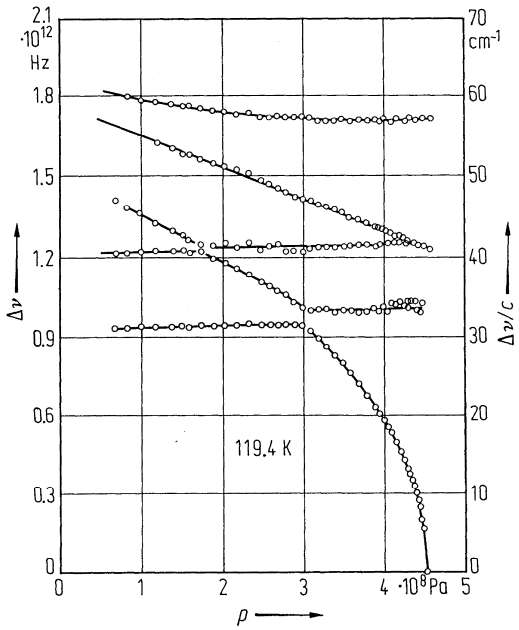

Fig. 20A-7-060. SbSI. $\Delta\nu$ vs. p at 119.4 K [76Pee]. p: hydrostatic pressure. $\Delta\nu$: Raman frequency shift of low frequency A_1 modes.

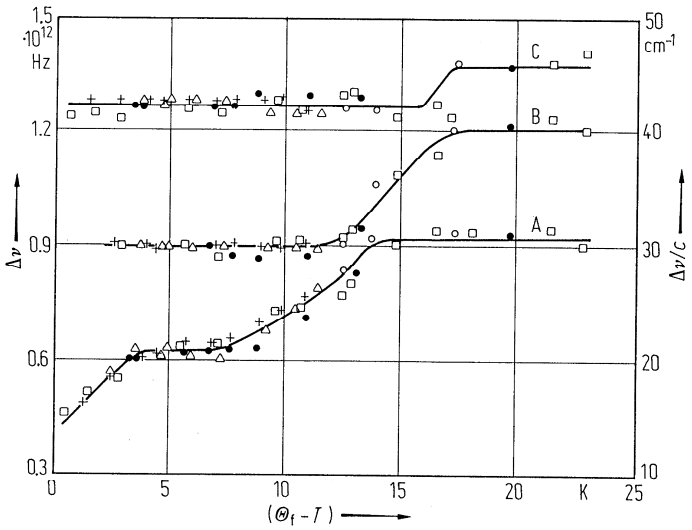

Fig. 20A-7-061. SbSI. $\Delta\nu$ vs. $(\Theta_f - T)$ [72Ten]. $\Delta\nu$: Raman scattering frequency shift for the three lowest frequency optical modes A, B, C. T = 0 °C (closed circles), 1.5 °C (triangles) and 3 °C (crosses and open circles) and the variation of $\Theta_f - T$ was induced by hydrostatic pressure. Squares: at $p = 200 \cdot 10^5$ Pa.

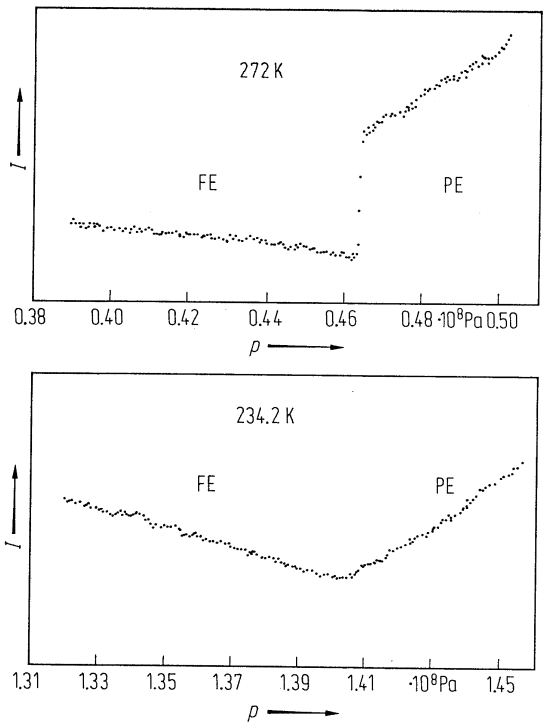

Fig. 20A-7-062. SbSI. I vs. p [76Pee]. I: intensity of elastic light scattering obtained by measuring the transmitted light. p: hydrostatic pressure. Continuous change of I was observed for $T_{crit} \leq 235$ K and $p_{crit} \geq 1.40 \cdot 10^8$ Pa. Upper figure: for 272 K and lower figure: for 234.2 K. FE and PE indicate ferroelectric and paraelectric phase, respectively. See also [75Pee].

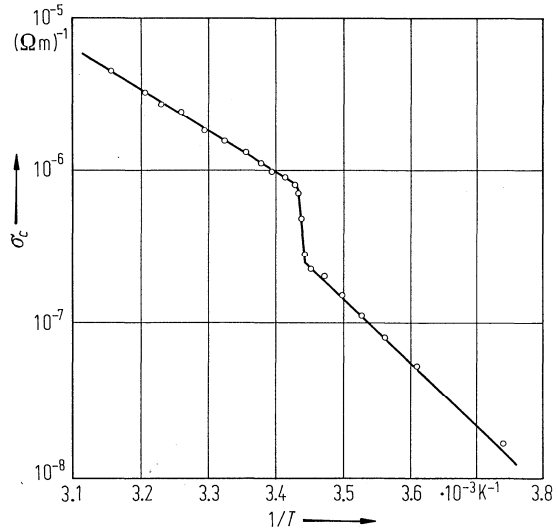

Fig. 20A-7-063. SbSI. σ_c vs. $1/T$ [86Toy]. σ_c: electric conductivity along c axis, with dc field of 30 kV/m. Activation energies: 0.52 eV ($T > \Theta_f$), 0.81eV ($T < \Theta_f$), $\sigma_c \propto \exp(-E_G/kT)$.

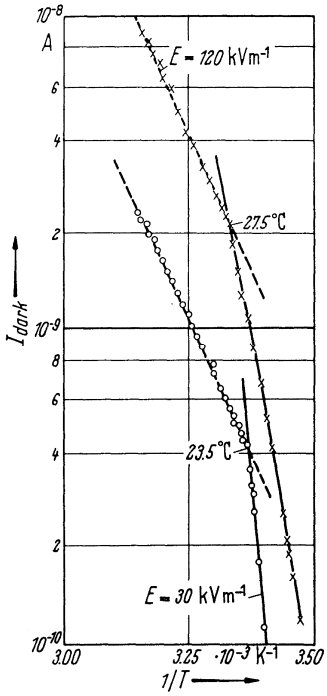

Fig. 20A-7-064. SbSI. Dark current I_{dark} vs. $1/T$ [65Sas]. Parameter: E, applied field along c axis.

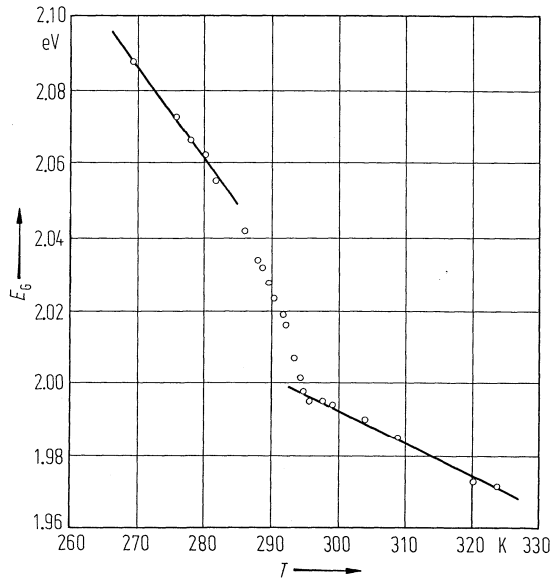

Fig. 20A-7-065. SbSI. E_G vs. T [82Gra]. E_G: forbidden band width obtained from thermomodulated spectroscopy. $dE/dT = -2.51 \cdot 10^{-3}$ eV K^{-1} ($T < \Theta_f$) and $-8.8 \cdot 10^{-4}$ eV K^{-1} ($T > \Theta_f$). Unpolarized light on (110) face.

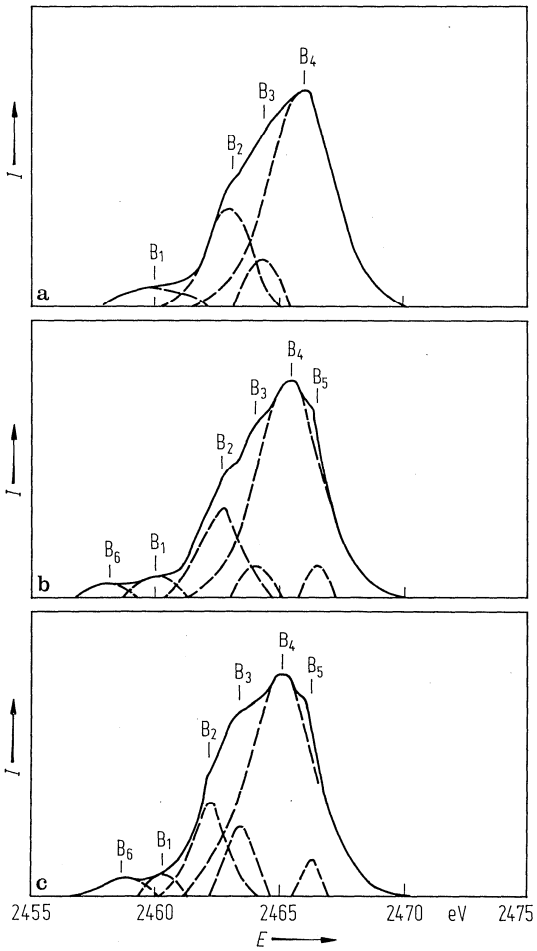

Fig. 20A-7-066. $SbS_xSe_{1-x}I$. Fluorescent X-ray spectra (intensity distribution) from K-bands of sulfur [85Suk]. (**a**) x = 1.0; (**b**) x = 0.75; (**c**) x = 0.25. Principal peak B_4 (x = 1.0, SbSI) corresponds to a density maximum of sulfur p-states forming the top of the valence band.

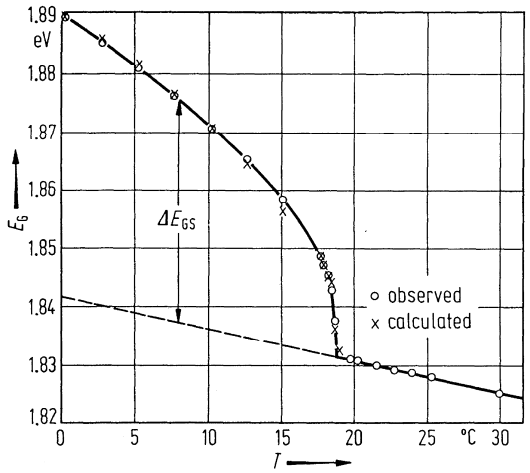

Fig. 20A-7-067. SbSI. E_G vs. T for light polarized parallel to the c axis [72Ish]. E_G: absorption edge defined as the photon energy whose absorption coefficient is 10^{-4} m. The spontaneous shift ΔE_{GS} is obtained by subtracting the extrapolated values of the linear term in the phase I from the observed edge energy in the ferroelectric region.

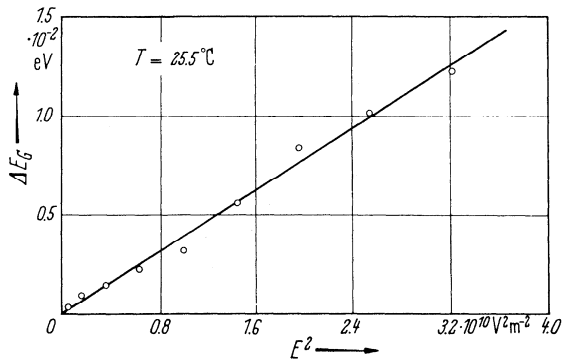

Fig. 20A-7-068. SbSI. ΔE_G vs. E^2 in the paraelectric phase [63Har]. ΔE_G: increase of the absorption edge energy E_G due to a dc field applied along the c axis.

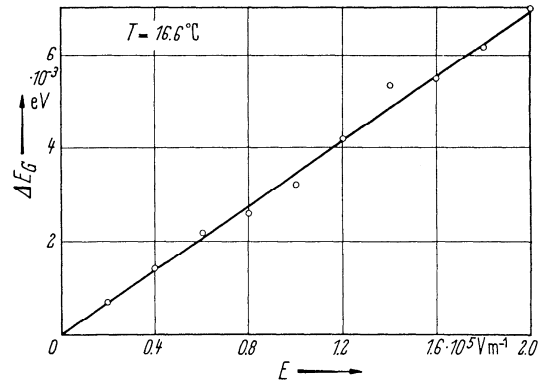

Fig. 20A-7-069. SbSI. ΔE_G vs. E in the phase I [63Har]. Compare Fig. 20A-7-068.

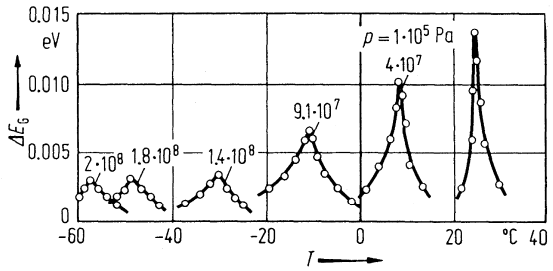

Fig. 20A-7-070. SbSI. ΔE_G vs. T [69Ger]. Parameter: p. ΔE_G: absorption edge shift induced by a constant electric field of $2 \cdot 10^5$ V m^{-1}.

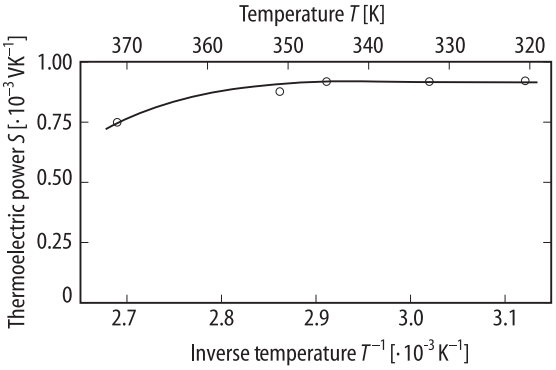

Fig. 20A-7-071. SbSI. Thermoelectric power S vs. $1/T$ [70Toy].

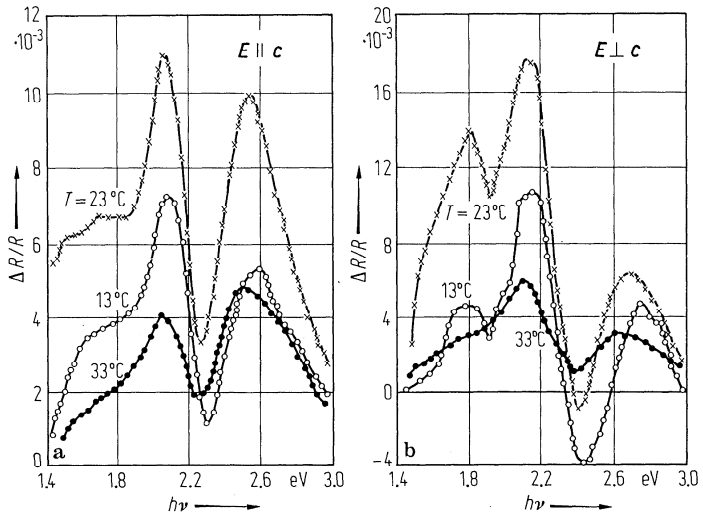

Fig. 20A-7-072. SbSI. $\Delta R/R$ vs. photon energy $h\nu$ [70Gol]. $\Delta R/R$: electroreflectance. Parameter: T. The electric vector of incident light is (**a**): parallel to the c axis, (**b**): perpendicular to the c axis.

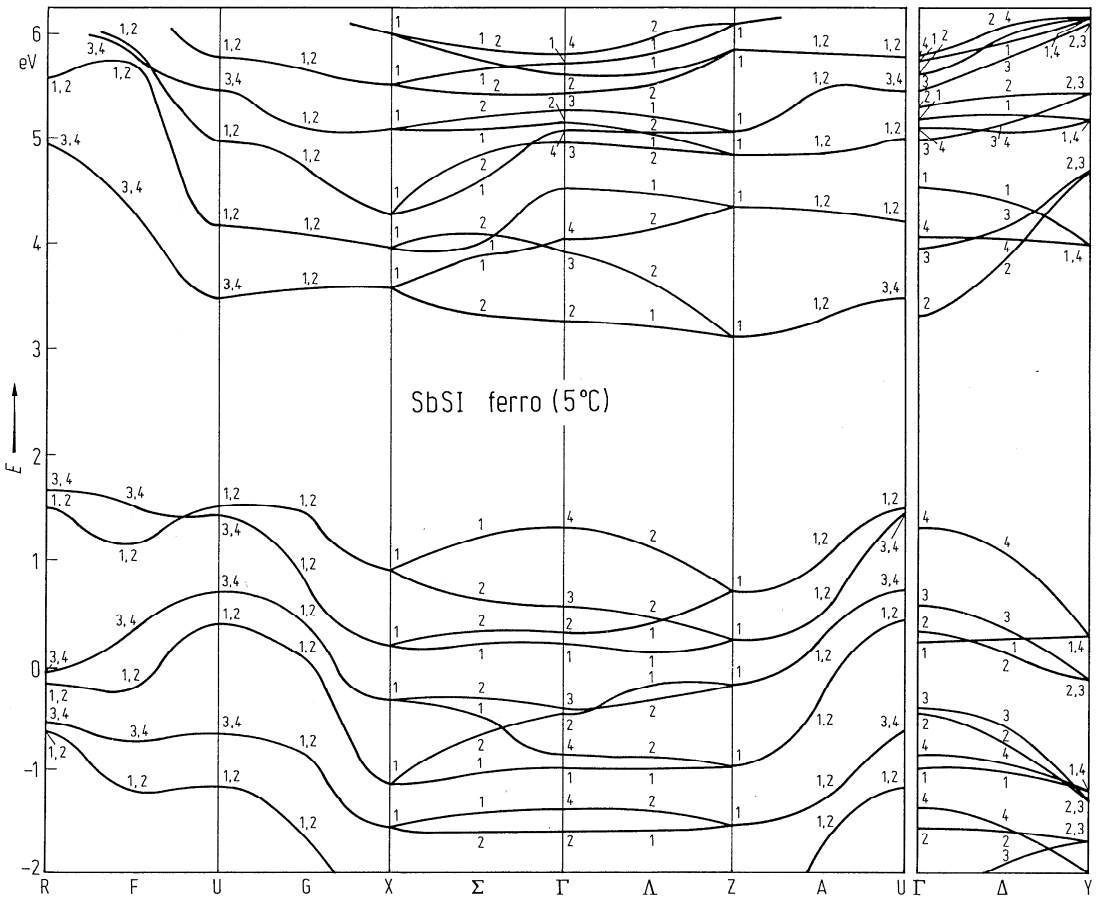

Fig. 20A-7-073. SbSI. Calculated band structure of phase I [73Nak]. Atomic positions at 35 °C and pseudopotential method are used.

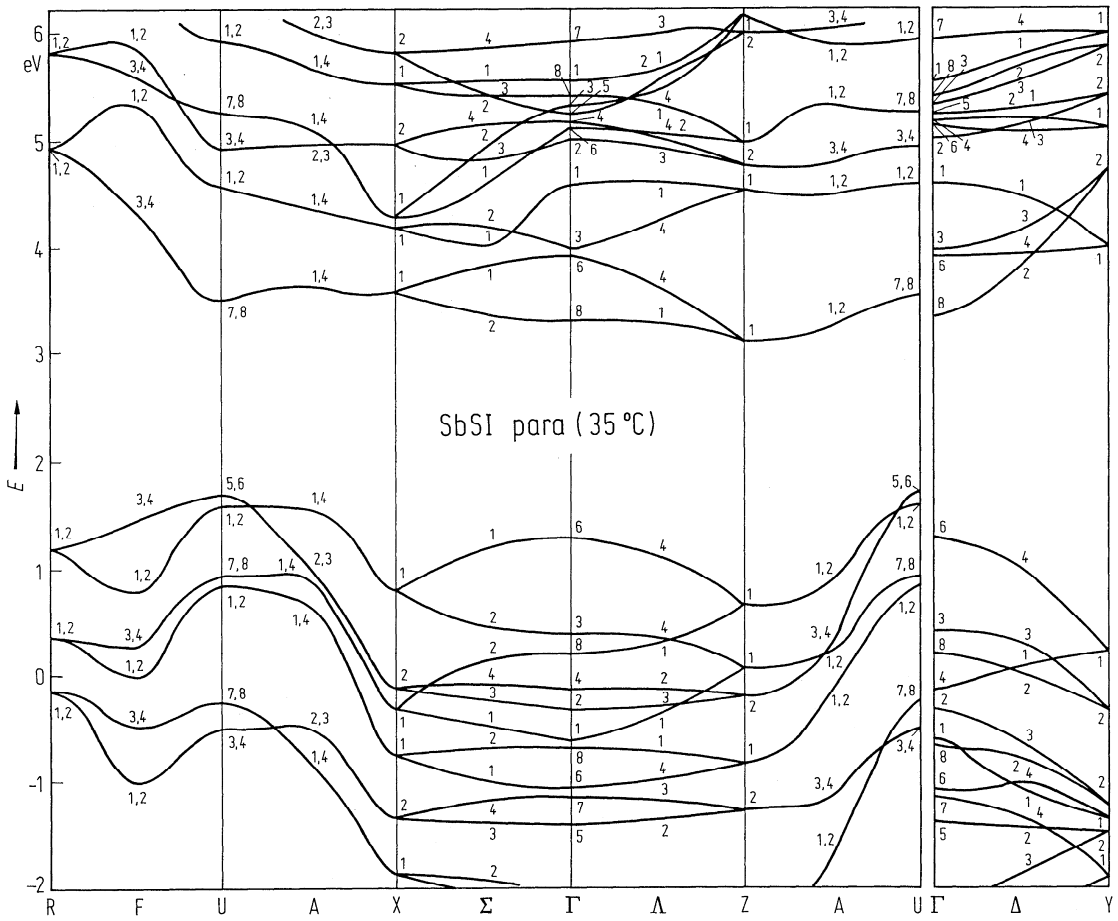

Fig. 20A-7-074. SbSI. Calculated band structure of phase II [73Nak]. Atomic positions at 5 °C and pseudopotential method are used.

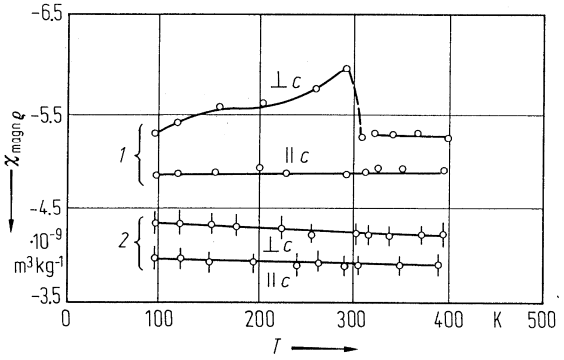

Fig. 20A-7-075. SbSI, BiSeI. $\chi_{magn\,\rho}$ vs. T [75Ber]. Curves *1*: SbSI; curves *2*: BiSeI.

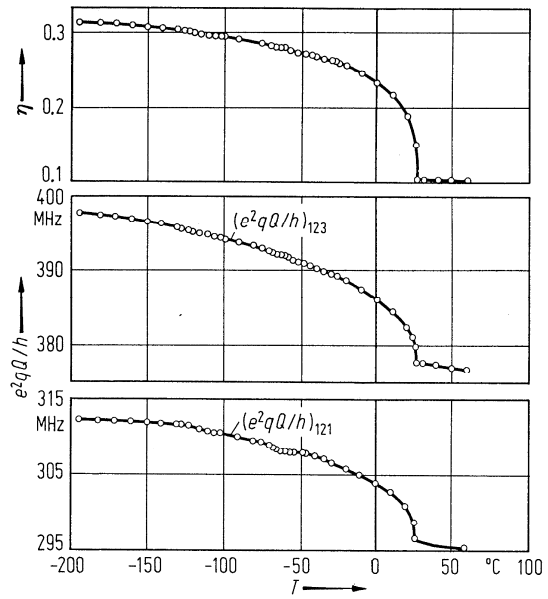

Fig. 20A-7-076. SbSI. e^2qQ/h, η vs. T [70Pop4]. $(e^2qQ/h)_{123}$ and $(e^2qQ/h)_{121}$ are quadrupole coupling constants for ^{123}Sb and ^{121}Sb, respectively, η: asymmetry parameter.

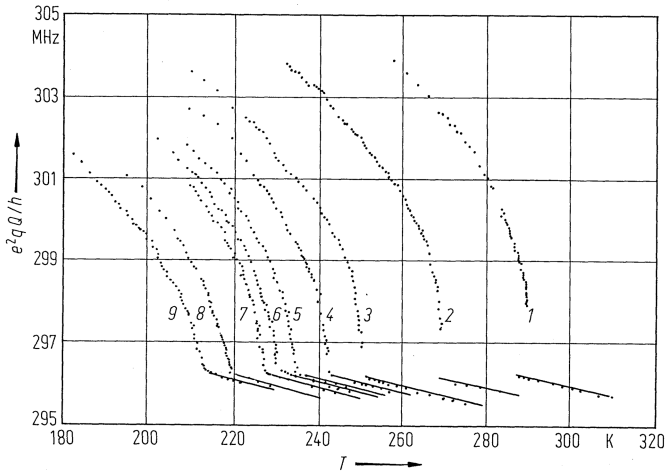

Fig. 20A-7-077. SbSI. e^2qQ/h vs. T [80Ale]. e^2qQ/h: nuclear quadrupole coupling constant of ^{121}Sb nuclei. Parameter: p [$\cdot 10^9$ Pa]. *1*: 10^{-4}, *2*: 0.05, *3*: 0.1, *4*: 0.12, *5*: 0.14, *6*: 0.15, *7*: 0.16, *8*: 0.18, *9*: 0.2.

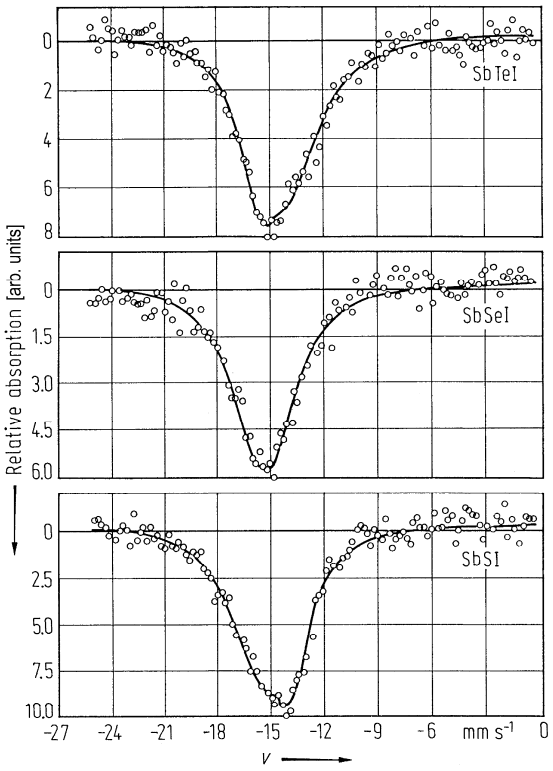

Fig. 20A-7-078. SbSI, SbSeI, SbTeI. Mössbauer spectrum [75Don]. v: source velocity of $Ba^{121}SnO_3$, $T = 4.2$ K.

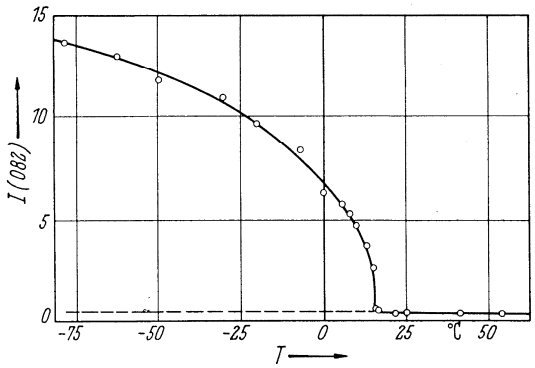

Fig. 20A-7-079. SbSI. $I(082)$ vs. T [67Tak]. I (082): integrated X-ray intensity of the (082) Bragg reflections [arbitrary unit].

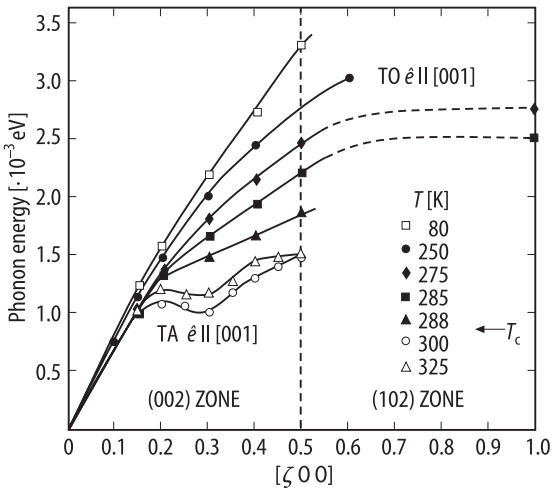

Fig. 20A-7-080. SbSI. Dispersion relation of [100] transverse acoustic and transverse optic modes [79Pou]. Parameter: T. $\hat{e}$: polarization direction of the modes.

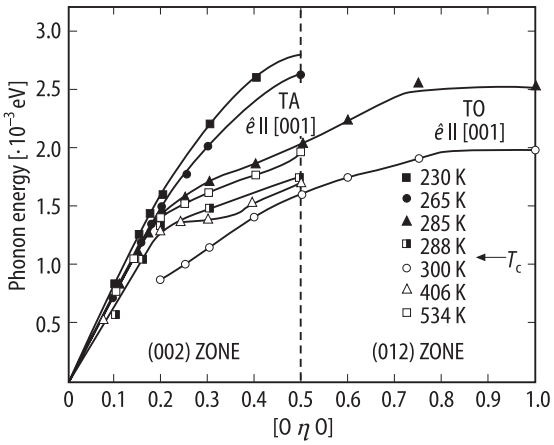

Fig. 20A-7-081. SbSI. Dispersion relation of [010] longitudinal acoustic, transverse acoustic and transverse optic modes [79Pou]. Parameter: T. $\hat{e}$: polarization direction of the modes.

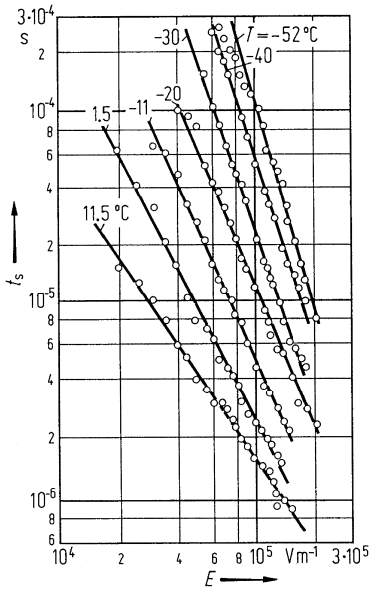

Fig. 20A-7-082. SbSI. Switching time t_s vs. E [70Kud]. Parameter: T.

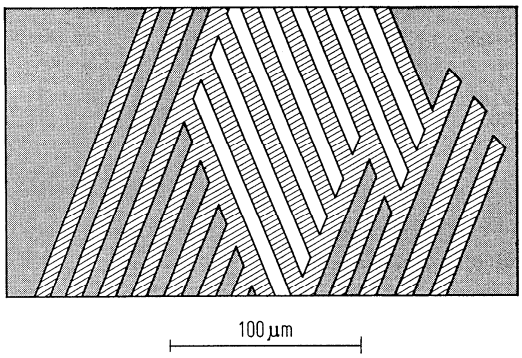

Fig. 20A-7-083. SbSI. "Fish bone pattern" observed at 25 °C [70Haf]. Sample thickness = 130 µm.

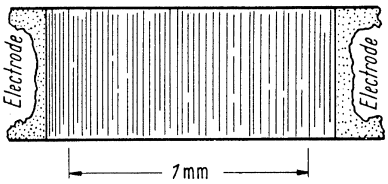

Fig. 20A-7-084. SbSI. Stripe pattern observed on (110) face at 15 °C under a dc field and light illumination ($\lambda \approx 640$ nm) [66Saw].